Postprint of: Bruski D., Burzyński S., Witkowski W., Analysis of passenger car crash with a cable barrier installed with anti-glare screens on a horizontal convex road curve with 400 m radius, International Journal of Impact Engineering, Vol. 173 (2023), 104486, DOI: 10.1016/j.ijimpeng.2022.104486

Analysis of passenger car crash with a cable barrier installed with anti-glare screens on a horizontal convex road curve with 400 m radius

Dawid Bruski[1*], *Stanisław* Burzyński[1], and *Wojciech* Witkowski[1]

[1] Gdańsk University of Technology, Faculty of Civil and Environmental Engineering, Department of Mechanics of Materials and Structures, Gabriela Narutowicza 11/12, 80-233 Gdańsk, Poland
* Coresponding author, dawid.bruski@pg.edu.pl

Abstract. High-tension cable barriers have been used on roads for a relatively short period compared with other types of road barriers. Hence, there remains a need for further research on various crash scenarios. An important issue is the performance of a cable barrier on a road curve, particularly when a vehicle impacts the convex side of the barrier. To address this issue, the analysis in this study considers a system of anti-glare screens installed on a cable barrier that is often used on the horizontal curves of roads to protect drivers from the glare of the headlights of oncoming traffic. The responses of the cable barrier and car are evaluated based on a full-scale crash test and a numerical simulation. The forces in the cables during impact and the influence of the anti-glare screens on the behavior of the cables are also investigated. Additionally, an analysis of the energy absorbed by the car and barrier subparts is performed. This study confirmed that cable barriers work properly and provide the highest level of safety; the study also showed that cables have a significant safety margin and the posts contribute most toward the total dissipated energy.

Keywords: cable barrier, anti-glare screen, TB32 crash test, simulation, energy absorption.

1. INTRODUCTION

1.1. Road cable barriers

Road safety barriers are one of the many road restraint systems (RRS) installed along roads. They serve to prevent an errant vehicle from leaving the road and hitting another car or an obstacle. Road safety barriers are used based on the premise that hitting a barrier is less dangerous than hitting a roadside hazard (Zou et al., 2014). Road barriers can be divided into three groups depending on their lateral stiffness: flexible barriers (e.g., cable barriers), semi-rigid barriers (e.g., w-beam guardrail barriers), and rigid barriers (e.g., concrete barriers) (Zou et al., 2014). Road cable barriers are flexible, and in general, these systems deflect more than the systems from the other two groups. This can help reduce the negative effects on vehicle occupants in the case of a collision. The major components of cable barrier systems are wire ropes, posts, cable-to-post attachments, and end anchors. Most modern cable barriers use three or four cables (Sheikh et al., 2008). A cable barrier, like any other road safety barrier, should minimize the negative consequences of road user errors in a manner that does not cause fatalities or serious injuries. If correctly designed and installed, it should contain and redirect an impacting car back onto a road, and this car should continue its motion approximately parallel to the barrier face and traffic flow, which minimizes the risk of a secondary collision.

Cable barriers were one of the first safety barrier systems used on roads. For instance, cable barriers have been used on U.S. highways since at least the 1920s (Ray et al., 2009). The first systems of cable barriers were low-tension systems, also referred to as generic systems. In these systems, only the cables are tensioned to eliminate the sag between the posts. In the 1980s, the British company Brifen developed a high-tension cable

barrier system (Marzougui et al., 2012). In high-tension systems, the cables are tensioned to an appropriate level, usually between 10 and 35 kN. This allows for the reduction in cable deflection during an impact; the deflection is much smaller than that for the low-tension systems (Zou et al., 2014). However, the high-tension cable barriers were not used in the United States until 2000 (Marzougui et al., 2012). In 2001, Brifen received approval from the Federal Highway Administration to begin marketing and installing its cable barrier system in the United States (Ray et al., 2009). As indicated in the study by Zou et al., many past investigations did not consider the high-tension cable barriers due to the short period of their usage at the time when these studies were being conducted (Zou et al., 2014).

Cable barriers are relatively inexpensive devices that are easy to install, maintain, and repair after collision (Cooner et al., 2009). They are often considered beneficial in terms of vehicle occupant safety (Bruski et al., 2019). Cable barrier systems that are installed on medians are called cable-median barriers (CMBs), and they can successfully contain impacting vehicles and significantly reduce fatal cross-median crashes (Ray et al., 2009; Stamatiadis et al., 2021). Furthermore, CMBs can properly contain vehicles for which barriers have not been designed (Cooner et al., 2009). An example of a high-tension cable barrier installed on a median strip is shown in Fig. 1-a. One of the most important issues is the analysis of the behavior of cable barriers on the horizontal curves of roads (Alberson et al., 2003; Marzougui et al., 2012). The horizontal curvature affects the value of the deflection of the cables in vehicular collisions, particularly when a car crashes into the convex side of a barrier. Research on such impacts with cable barriers has already been published (e.g., (Alberson et al., 2003; Marzougui et al., 2012; Schmidt et al., 2013; Wilde et al., 2019); however, the number of such studies is still limited. It should be noted that when a safety barrier is installed on a horizontal road curve, a system of anti-glare screens is often installed on that barrier. These screens are intended to prevent a driver from the glare of the headlights of oncoming vehicles. An example of such a device is shown in Fig. 1-b. The analysis of the behavior of a cable barrier system with anti-glare screens installed on a horizontal road curve during a vehicular collision remains uninvestigated. However, real-life accidents with cable barriers and anti-glare screens can be observed, as shown in Fig. 2. In this particular case, the damage to the system, including the deflection of a few posts and the sliding of several screens, implies that the impact energy was not significant. Notwithstanding, the question remains about how that system would have behaved and how the anti-glare screens would have affected the crash outcome if the impact energy was higher.

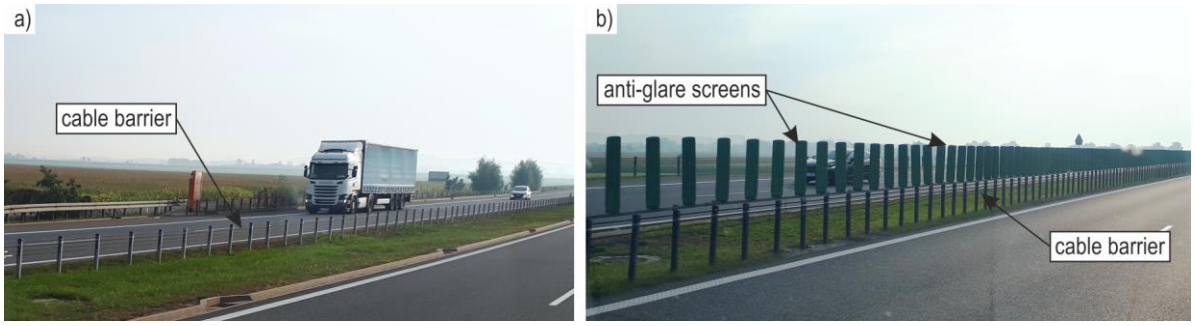

Fig. 1 Photographs of road-safety barriers: a) cable barrier and b) cable barrier with anti-glare screens.

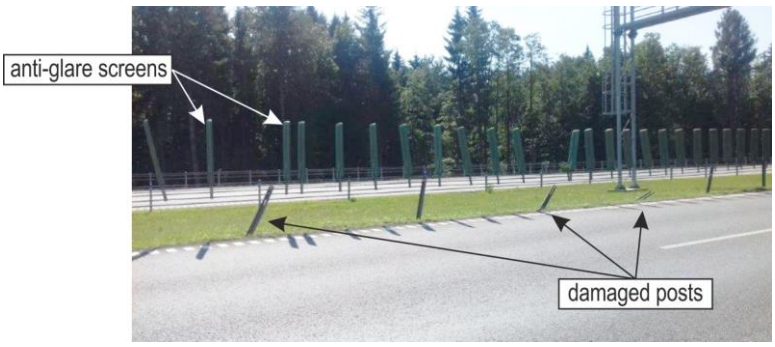

Fig. 2 Photograph of a damaged cable barrier with anti-glare screens (source: GDDKiA, Poland).

1.2. Literature review

The performance and effectiveness of road-safety barriers must be evaluated by conducting full-scale crash tests. In Europe, the EN 1317 standard has been used to evaluate RRSs ("PN-EN 1317-1:2010. Road restraint systems – part 1: Terminology and general criteria for test methods," 2010, *PN-EN 1317-2:2010. Road restraint systems – part 2: Performance classes, impact test acceptance criteria and test methods for safety barriers including vehicle parapets*, 2010, "PN-EN 1317-5+A2:2012. Road restraint systems – part 5: Product requirements and evaluation of conformity for vehicle restraint system," 2012). This standard defines the impact criteria for 11 crash tests. Five out of the 11 tests involve passenger cars weighing 900, 1,300, and 1,500 kg. Depending on the crash test, the impact velocity, impact angle, type, and mass of the vehicle are varied. The performance classes of a road-safety barrier are determined based on three criteria: the containment level, working width, and impact severity level. These criteria are assessed using full-scale crash tests.

The first criterion is the containment level, which allows for the assessment of the capacity of a barrier to restrain an impacting vehicle. Four containment levels were distinguished: low, normal, high, and very high.

The second performance class was the working width (W_m). This index allows for the evaluation of the deformation of a barrier during a vehicle collision. The working width is defined as the maximum lateral distance between any part of the barrier on the undeformed traffic side and the maximum dynamic position of any part of the barrier or a vehicle if the vehicle body deforms around the parts of the barrier. Another important index that allows for the assessment of barrier deformation is dynamic deflection (D_m). This index is determined based on the maximum dynamic displacement of any point on the barrier traffic face during a collision. These two indices, the working width and dynamic deflection, allow one to assess an obstacle-free zone behind a barrier to enable it to work properly during an accident.

The third performance class is the impact severity level. It is used to estimate the severity of a crash and anticipate vehicle occupant injuries as a result of a collision. The impact severity level is determined based on two indices: the acceleration severity index (ASI) and the theoretical head impact velocity (THIV). These indices should be determined for the cars. ASI(t) is a non-dimensional function of time calculated using the filtered components of the accelerations along the three axes (x, y, and z), which are recorded near the center of gravity of a car. The maximum value of the function of $ASI(t)$ during a crash is considered the ASI value, that is, ASI = max[ASI(t)]. The second index for determining the impact severity level is the THIV. The THIV concept is as follows. An occupant is considered a freely moving point called the theoretical head (TH). It is assumed that TH has the same velocity as that of the car at the moment of impact. Next, as a result of the impact, the car starts rotating and changing its speed, but the TH continues moving in a straight line until it hits the theoretical surface of the interior of the car. The speed of the TH at the moment of contact with the car cockpit is considered the THIV value. Additionally, one can calculate the length of the flight of TH relative to

the car, as well as the duration of that flight. If in the test ASI ≤ 1.0 and THIV ≤ 33 km/h, it is assumed that the tested barrier ensures the highest level of safety for vehicle occupants.

In addition to the above indices, which allow for the determination of the three performance classes of a road barrier, other indices and criteria were also determined. The first is the criterion for the exit box. This allows the behavior of a vehicle to be checked after its departure from a barrier. It is assumed that the impacting vehicle after leaving a barrier should continue its movement within the area defined as the "exit box". The dimensions of this area depend on the type and dimensions of the vehicle. The deformation of a car was also examined and assessed using the vehicle cockpit deformation index (VCDI), which was determined by the location and measurement of the deformation of the passenger compartment. The length and duration of the contact between a barrier and a car, the number of damaged posts, the length of the damage, the maximum permanent deflection of the barrier, and others can also be determined. All these data can be very useful, especially in the context of the verification and validation (V&V) of numerical calculations ("PN-EN 16303:2020. Road restraint systems - Validation and verification process for the use of virtual testing in crash testing against vehicle restraint system," 2020).

Currently, full-scale crash testing is the most reliable method for evaluating the performance of road barriers, although there is no guarantee of the success of these devices in real-world accidents (Ray et al., 2009). It should be also noted that crash tests defined in the EN1317 standard do not cover the entire range of accidents that may happen on roads. Thus, there is a constant need for research on the performance of road safety barriers under various impact conditions. In addition to full-scale crash tests, numerical simulations are a useful tool for evaluating the performance of RRS (Budzyński et al., 2022; Chen et al., 2015; Klasztorny et al., 2018; Reid et al., 2009; Teng et al., 2016; Uddin, 2004; Wolny et al., 2022; Wu and Thomson, 2007). There has been much research on road barriers using both experimental and numerical tests, but only a few of them are concerned with cable barriers.

Mohan et al. (Mohan et al., 2005) developed a finite element model and performed a simulation of a low-tension CMB. The simulation was validated against a full-scale crash test. This model was able to accurately recreate the behaviors of the barrier and vehicle. Additionally, the authors investigated four issues related to cable barrier modeling: soil–post, post–hook, cable–hook, and cable–vehicle interactions. Marzougui et al. (Marzougui et al., 2009) analyzed the effects of the spacing of the end anchor and the initial tension in the cables on the deflection of the barrier. They considered the different numbers of cables (three or four) and their arrangement (parallel or interwoven). The results revealed that the greater the anchor spacing, the greater is the cable deflection during a collision. The arrangement of the cables also affects the barrier performance. The study also showed that the initial value of the tension on the cables affected the results, but to a much lesser degree than the other investigated variables. Bi et al. (Bi et al., 2010) studied the performance of a low-tension CMB on sloped medians. The results indicated that the height of the cables had an effect on the barrier behavior in a sloped terrain. The research team led by professor Reid (Reid et al., 2010; Stolle and Reid, 2011) developed a numerical model for wire ropes used in cable barriers. The authors conducted many experimental and numerical tests that enabled them to determine the properties of a 3 × 7 19 mm wire rope. This research also included a comparison of the results from the numerical simulation and the full-scale crash test. Schmidt et al. (Schmidt et al., 2013) performed and analyzed three full-scale crash tests on low-tension cable barrier systems, which were installed on road curves with radii of 110 and 134 m. Wang et al. (Wang et al., 2013) presented and evaluated numerical models for cables and hooks used in a cable barrier system. Fang et al. (Fang et al., 2015) analyzed various crashes in a low-tension CMB using a validated numerical model. The research included several cable barrier designs under various impact conditions. Bruski et al. (Bruski et al., 2019) analyzed the vehicular impact into a high-tension cable barrier at a low impact angle using a full-scale crash

test and numerical simulation. Their study also presented the validation process for the numerical model. Wilde et al. (Wilde et al., 2019) studied the behavior of a high-tension cable barrier system installed on a horizontal road curve. Various impact velocities, impact angles, and road curves were considered. Based on the simulation, the analyzed cable barrier was found to be a safe system for car occupants.

As mentioned above, most studies have been conducted on low-tension cable barriers, and analyses of the performance of high-tension cable barriers on horizontal road curves are rare, particularly those based on experimental and numerical crash tests. Furthermore, many studies have not analyzed the stress state or axial forces in the cables. For instance, one can find information that the cable tensions at the end anchors during a crash could be 4 to 5 times as large as the tension before the impact (Marzougui et al., 2012). To the best of the authors' knowledge, there is no research that incorporates a full-scale crash test and numerical simulation for a high-tension cable barrier installed on a road arc. In addition, none of these studies considered the influence of the installation of anti-glare screens on the behavior of a cable barrier. These screens are often mounted on a barrier on a road curve to prevent drivers from blinding caused by the headlights of oncoming traffic.

1.3. Aim, scope, and significance of research

This study aims to analyze the crash of a passenger car with a 3-cable high-tension barrier system installed with anti-glare screens placed on a horizontal convex curve on a road with a radius of 400 m. The less favorable case of an impact is considered, that is, the impact on the convex side of the curved barrier. The impact conditions corresponded to the TB32 crash test, that is, the impact speed was 110 km/h, impact angle was 20º, and mass of the car was 1,500 kg (*PN-EN 1317-2:2010. Road restraint systems – part 2: Performance classes, impact test acceptance criteria and test methods for safety barriers including vehicle parapets*, 2010).

The scope of the study includes the following: (1) developing a numerical model and validating it against the full-scale crash test; (2) determining and analyzing the results from both the full-scale and numerical tests; (3) examining the extent of the damage to the barrier and car; (4) analyzing the forces in the cables during the impact; (5) investigating the influence of the anti-glare screens on the barrier behavior; and (6) performing the energy analysis, including the determination of the amount of absorbed energy.

The results of this study are expected to broaden our understanding of the response of high-tension cable barriers installed on road curves. The simulation provides detailed insights into the complex mechanisms of the impact. This investigation is expected to be useful in evaluating the influence of adding anti-glare screens on the behavior of cables. The study of the axial forces in the cables allows for the assessment of the safety margin in wire ropes in a common crash with a 1,500-kg passenger car. Additionally, the analysis of the redistribution of the impact energy indicates the most important barrier parts from the perspective of energy absorption. Such information could be helpful, for example, in the selection of barrier parts and design variables in an optimization process (Honda et al., 2021; Yin et al., 2017, 2016). It is also worth emphasizing that the use of a full-scale crash test and the corresponding simulation substantially increases the reliability of the analyses. In addition, a comparison of the results from the simulation and the actual test allows for the assessment of the viability and accuracy of the applied methods of numerical modeling.

2. CRASH TEST AND NUMERICAL MODEL

2.1. Cable barrier and full-scale crash test

In this study, the N2/W4/A class high-tension cable barrier was tested in the field. Photographs of the barrier, course of the crash test, and crash results are presented, discussed, and compared with the results from a numerical simulation in the following sections.

The barrier comprised three 3 × 7 19 mm wire ropes mounted on C-posts. The top wire rope was installed 0.73 m above the ground level. The distance between the two top cables was 80 mm, and the distance between the two bottom cables was 160 mm. The initial pre-tension force of the wire ropes was 25.5 kN and was introduced at the turnbuckles between post nos. 7 and 8. Strain gauges were installed on the turnbuckles to enable strain measurements during the impact. The ends of the cables were connected to massive concrete blocks. The cable-to-post attachment consisted of hooks. U-shaped hooks with a diameter of 5 mm were used. The details of the cable-to-post attachment are shown in Fig. 3-e. The length of the single posts was 1.7 m. For the horizontal section, the posts were embedded in the soil at a depth of 0.93 m. The spacing of the post was 2.0 m. Two end posts at both ends of the systems were equipped with additional steel plates, which stabilized the post in the soil. The total number of posts was 29. The posts were numbered from 0 to 28 according to the direction of vehicle movement. Post caps were placed at the top of each post. Additional anti-glare screens were installed on the cables. The spacing between the screens was 0.67 m, that is, there were three screens between two consecutive posts. The total length of the barrier was 67.7 m, 52.0 m in the horizontal section, and two end terminals, each 7.85 m long.

A full-scale crash test of the cable barrier was conducted at the Research Institute for Protective Systems (www.ibos.com.pl) in Inowrocław, Poland by the Road and Bridge Research Institute (www.ibdim.edu.pl) on August 30, 2017. The crash test was conducted as a part of the RID 3A research project "Road Safety Equipment."

The impact conditions of the test were chosen as in the TB32 crash test, that is, the impact speed was 110 km/h, impact angle was 20º, and car mass was 1500 kg (*PN-EN 1317-2:2010. Road restraint systems – part 2: Performance classes, impact test acceptance criteria and test methods for safety barriers including vehicle parapets*, 2010). The 1990 BMW 520 e34 was used for the full-scale crash test. The actual mass of the car was 1444.2 kg. During the test, a cable barrier was installed on a horizontal arc with a radius of 400 m. The car crashed into the convex side of the arc. The critical impact point was selected at about one-third of the installation length, which was 1.3 m upstream the post no. 10. The actual impact velocity and angle were 112 km/h and 19.8°, respectively.

2.2. Numerical model of crash test

The numerical model of the crash test consisted of a road cable barrier with anti-glare screens mounted on ropes, the ground under each post, a car, and the horizontal surface on which the car was moving. The LS-DYNA software package was used to perform the numerical simulations (Hallquist, 2006). Numerical simulations are a useful tool for evaluating and analyzing the behavior of road safety equipment (Fang et al., 2021; Pachocki and Bruski, 2020). The most important aspects of the numerical model of the crash test are as follows.

2.2.1. Road cable barrier

A numerical model of the cable barrier, ground, and road surface was developed. The model is illustrated in Fig. 3. The model of the barrier included cables, turnbuckles, posts, post caps, and hooks. Anti-glare screens

were mounted on the cables. The barrier parts and screens are shown in Fig. 3-b. The average size of the shell finite elements (FEs) of the post was 14 mm, and that of the post caps was 16 mm. The length of the beam FEs for the cables was 12.5 mm. The cables were modeled based on the study by Reid et al. (Reid et al., 2010) The hooks were modeled with beam FEs of size 5 mm. The size of the shell FEs used to model the screens varied from 10 to 30 mm. The soil under each post was modeled using solid FEs with sizes varying from 20 to 130 mm. The details of the FE dimensions are presented in Fig. 3-c. The two outermost posts at each end of the barrier had an additional plate to help stabilize these posts in the soil. The cables were connected to the anchors. The outermost posts and anchors are shown in Fig. 3-d. A view of the cable-to-post attachments is shown in Fig. 3-e. The model of the barrier, screens, soil, and road surface consisted of 370,750 FEs, comprising 355,593 nodes. The geometry and dimensions of the numerical model corresponded to the dimensions of the actual barrier presented in Section 2.1. A cable barrier was installed on the horizontal road curve with a radius of 400 m. A comparison between the numerical model and the actual system is shown in Fig. 3-a-b. The most important data for the computational model are presented in Tab. 1.

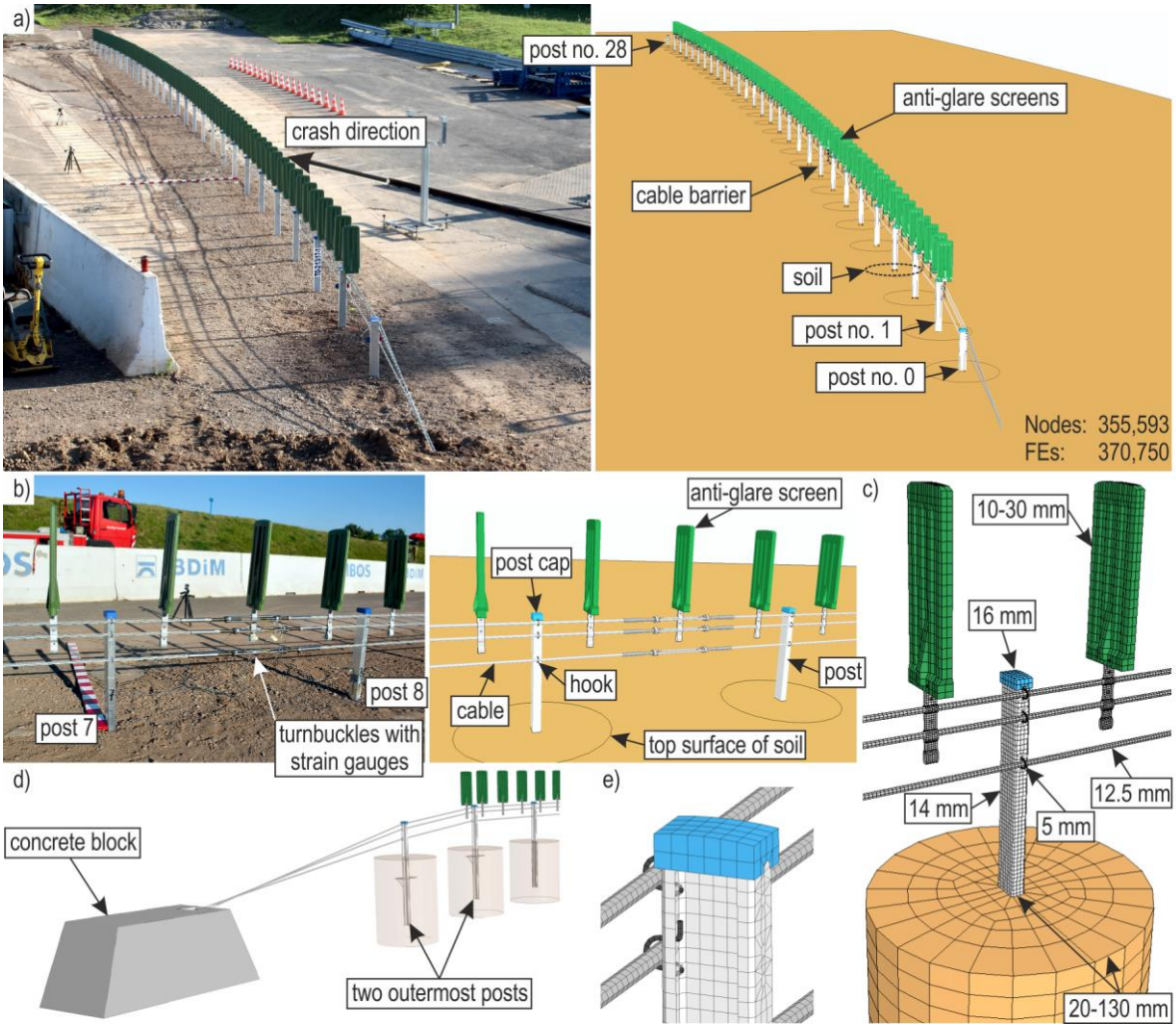

Fig. 3 Numerical model: a) general view and comparison with the actual model, b) parts of the model, c) mesh size of the parts, d) end of the barrier, and e) cable-to-post attachment.

Tab. 1 Summary of the computational model.

Part	Technical data	Model parameters
Cable	Three 3 × 7 19 mm (3/4 in.) wire ropes	Belytschko–Schwer resultant beam FEs; Elasto–plastic material model with piecewise linear isotropic hardening rule; Mass density = 4,161 kg/m^3; Young's modulus = 59.05 GPa;

		Force–strain, moment–curvature, and torque–twist rate curves based on the report by Reid[a]
Turnbuckle	Three turnbuckles between post nos. 7 and 8 Pretension force: 25.5 kN	Discrete beam/cable FEs; Elastic material model for cables (no forces in compression); Mass density = 7,850 kg/m^3; Young's modulus = 205 GPa.
Post	C100 steel post Length: 170 cm Thickness: 4 mm	Belytschko–Tsay shell FEs Elasto–plastic material model with isotropic hardening rule; Stress–strain curve obtained from tensile test Density = 7,850 kg/m^3; Young's modulus = 205 GPa; Poisson's ratio = 0.3; Yield stress = 344.8 MPa; Cowper–Symonds model applied for strain-rate effects
Hook	Diameter: 5 mm	Hughes–Liu beam FEs; Elasto–plastic material model with isotropic hardening rule; Material properties taken from NCAC[b] Yield stress = 498 MPa; Cowper–Symonds model applied for strain-rate effects
Post cap	No structural function	Belytschko–Tsay shell FEs; rigid material model
Anchor	Fully constrained (displacements and rotations)	Constant stress solid FEs; rigid material model
Anti-glare screen	Height: 0.60 m Width: 0.22 m Spacing: 0.67 m	Fully integrated shell FEs; Elastic material model Density = 953 kg/m^3; Young's modulus = 1000 MPa; Poisson's ratio = 0.3
Soil	Modeled as individual cylinders below each post Diameter: 1.0 m Height: 1.188 m	Constant stress solid FEs; Elasto–plastic material model for soils Density = 1,700 kg/m^3; Shear modulus = 49.5 MPa; Bulk modulus = 185 MPa; Constants for plasticity surface: A_0 = 0.012013 MPa^2, A_1 = 0 MPa, A_2 = 0 (pressure does not affect plasticity surface) Material properties taken from NCAC[b]
Road surface	Horizontal plane allowing vehicle movement	Belytschko–Tsay shell FEs; rigid material model

[a] (Reid et al., 2010)

[b] ("National Crash Analysis Center, http://www.ncac.gwu.edu/vml/models.html, date of access 10.03.2016," 2016)

2.2.2. Passenger car

For the full-scale crash test, the 1990 BMW 520 e34 car was used. The same model was applied in the simulation. This computational model was originally developed in France by the Transpolis (formerly LIER). The model was subjected to some modifications, including re-meshing of selected parts, addition of tire reinforcement, or addition of wing mirrors. Examples of this numerical model can be found in (Qian et al., 2016; Wilde et al., 2021). Most parts of the car were modeled using fully integrated shell elements, with the piecewise linear plasticity material model assigned to them. The numerical model consisted of 22,796 nodes, comprising 23,681 FEs. An accelerometer was mounted near the center of gravity in both the actual cars to determine the ASI and THIV. The actual car and the corresponding numerical vehicle model are shown in Fig. **4**. The detailed parameters of the actual and numerical vehicles, along with the EN 1317 requirements, are listed in Tab. 2.

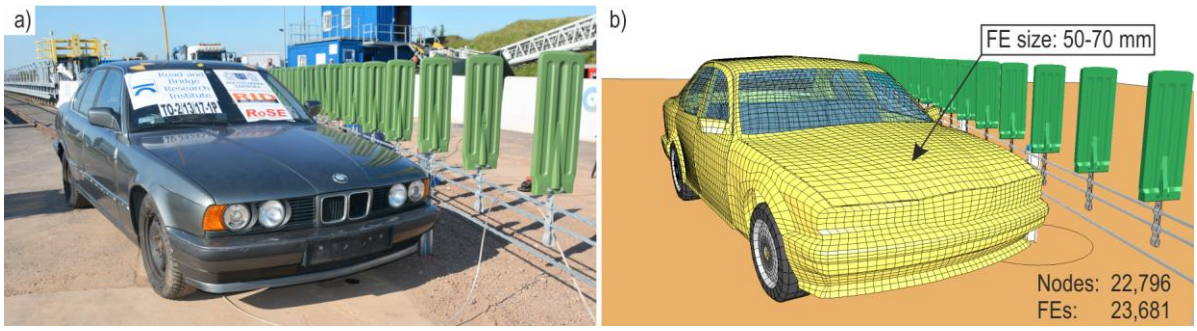

Fig. 4 Passenger car: a) actual vehicle and b) numerical model.

Tab. 2 Comparison of the parameters of the actual car and numerical car model.

Vehicle specifications	Full-scale crash test	Simulation	EN 1317	Requirement fulfillment
Ballast mass, kg	84 ± 2	0	≤180	Fulfilled
Total vehicle mass, kg	1,444.2 ± 2	1,505.4	1,500 ± 75	Fulfilled
Vehicle length, m	4.720 ± 0.020	4.714	n/a	n/a
Vehicle width, m	1.745 ± 0.020	1.774	n/a	n/a
Front-wheel track, m	1.420 ± 0.020	1.490	1.500 ± 0.225	Fulfilled
Rear-wheel track, m	1.475 ± 0.020	1.490	1. 500 ± 0.225	Fulfilled
Front-wheel radius, m	0.307 ± 0.005	0.295	n/a	n/a
Rear-wheel radius, m	0.295 ± 0.005	0.295	n/a	n/a
Wheel base, m	2.750 ± 0.005	2.761	n/a	n/a
CG_x[a], mm	1,322 ± 8	1,238.4 mm	1,240 ± 124 mm	Fulfilled
CG_y[b], mm	-5 ± 5	1.9 mm	± 80 mm	Fulfilled
CG_z[c], mm	550 ± 8	558,4 mm	530 ± 53 mm	Fulfilled

[a] CG_x: longitudinal distance from front axle to center of gravity
[b] CG_y: lateral distance from vehicle center line to center of gravity
[c] CG_z: height above ground to center of gravity

3. RESULTS AND DISCUSSION

3.1. Results of crash test and simulation

3.1.1. Crash test course

In the TB32 crash test with cable barrier installed on the road curve, the actual impact speed was 112 km/h and the impact angle was 19.8°. The impact kinetic energy of the test (also known as impact severity (*AASHTO MASH-2, Manual for assessing safety hardware (MASH), 2nd edition, American Association of State Highway Transportation Officials*, 2016)), calculated as the component of the vehicle kinetic energy perpendicular to the barrier face at the time of the impact, was 80.2 kJ. The car impacted the convex side of the barrier. The impact point was approximately 0.7 m after the post no. 9. In the simulation, the impact speed, angle, and location were the same as those in the crash test. The mass of the actual car was 1,444.2 kg, and in the simulation, it was 1,505.4 kg. After striking the barrier, the car was contained, redirected, and guided along the barrier by the wire ropes. The car then left the barrier at post no. 18. Subsequently, the car moved along the barrier and rotated along its vertical axis. The length of the car–barrier contact was 20 m, and the duration of contact was 0.71 s. In the simulation, these values were 17 m and 0.75 s, respectively. The barrier in the crash test and simulation fulfilled its most important task, that is, it contained and redirected the car back onto the road, and the cables did not break.

In the considered test, two collision phases can be distinguished. In the first phase, the car crashed the barrier and deformed until the working width value was reached. Subsequently, the second phase of collision was initiated. In this phase, the deflection of the cables was reduced, and the car was forced back on the road. The second phase ended when the car left the barrier. Subsequently, the vehicle moved away from the barrier and was no longer in contact with it. The vehicle trajectories in both the full-scale crash test and numerical simulation are presented in Fig. 5 and Fig. 6. It is assumed that the moment of impact of the vehicle into the barrier corresponds to time $t = 0.0$ s. A detailed presentation and discussion of the results are provided in the following sections.

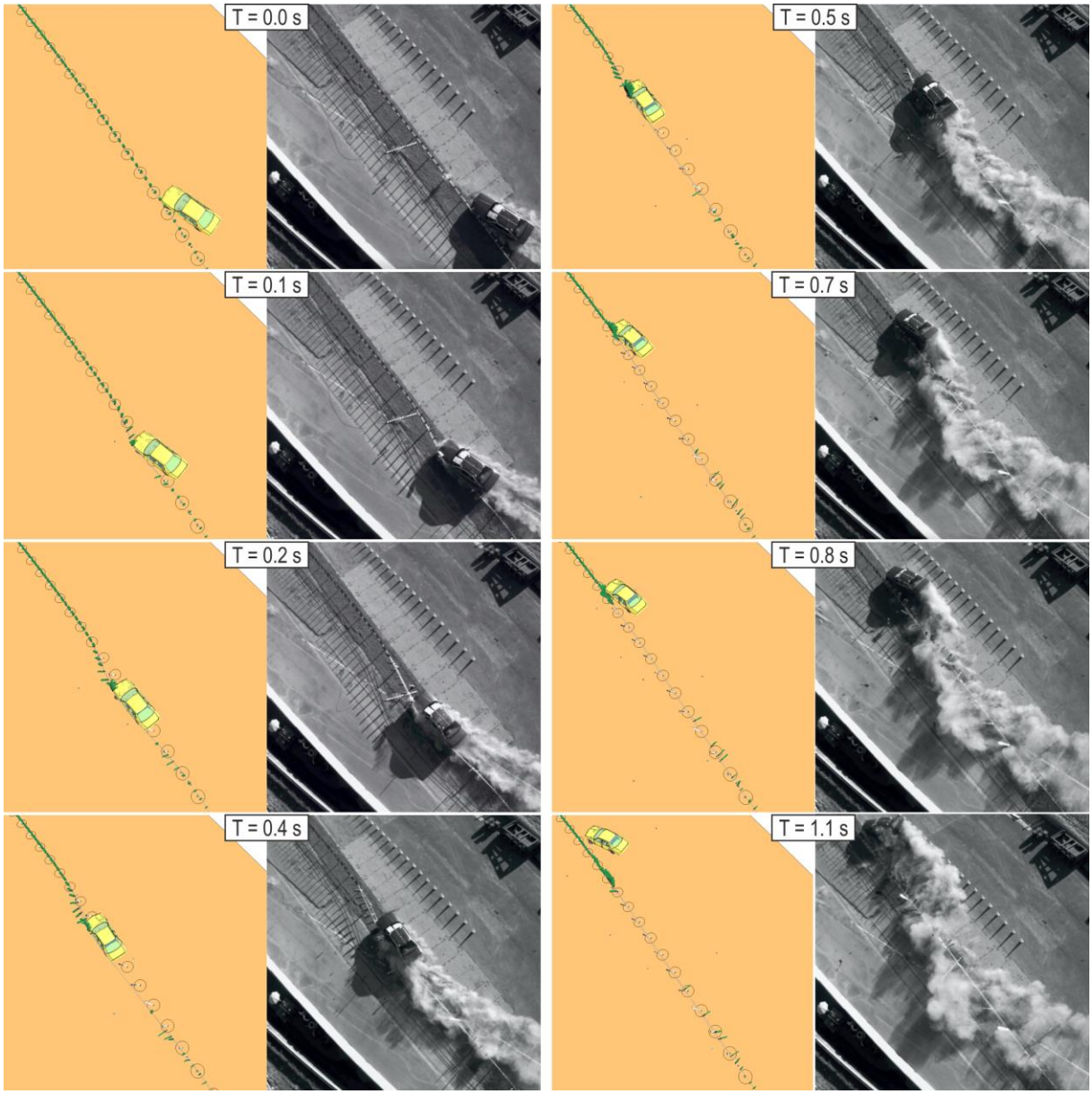

Fig. 5 Comparison of the trajectory of the vehicle from crash test and simulation: top view.

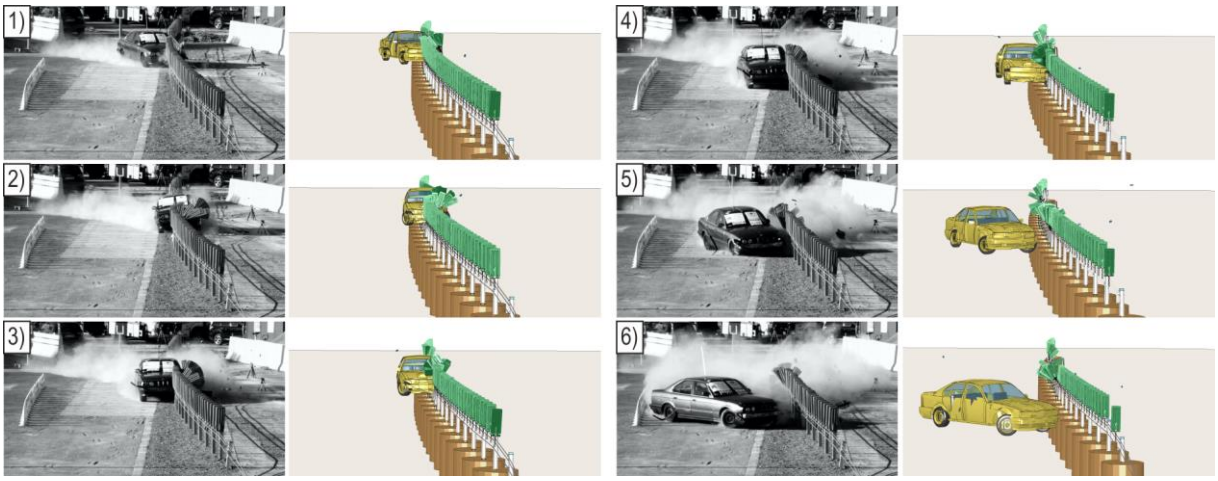

Fig. 6 Comparison of the trajectory of the vehicle from crash test and simulation: front view. Note: road surface is transparent to show the soil in numerical simulation.

3.1.2. Crash test results

The V&V of the numerical simulation was based on a comparison between the results of the crash test and the simulation. The criteria of the PD CEN/TR 16303 technical report were considered ("PN-EN 16303:2020. Road restraint systems - Validation and verification process for the use of virtual testing in crash testing against vehicle restraint system," 2020). Tab. 3 presents a comparison of the most important indices obtained from the crash tests and simulations. These results are discussed in the following paragraphs and sections of this article.

Tab. 3 Results of crash test and simulation

Test index	Full-scale crash test	Simulation
Working width W_m	1.13 ± 0.1 m	1.28 m
Working width criterion	n/a	$\|1.23\text{ m} - 1.13\text{ m}\| \leq (0.05\text{ m} + 0.1 \cdot 1.13\text{ m})$; fulfilled
Time of W_m occurrence	n/a	0.30 s
Dynamic deflection D_m	1.13 ± 0.1 m	1.23 m
Dynamic deflection criterion	n/a	$\|1.23\text{ m} - 1.13\text{ m}\| \leq (0.05\text{ m} + 0.1 \cdot 1.13\text{ m})$; fulfilled
Time of D_m occurrence	n/a	0.30 s
ASI	0.52	0.51
ASI criterion	n/a	$\|0.51 - 0.52\| \leq 0.1$; fulfilled
Time of ASI occurrence	0.24 s	0.28 s
Time of ASI occurrence criterion	n/a	$\|0.28\text{ s} - 0.24\text{ s}\| \leq 0.05$ s; fulfilled
THIV	19 km/h	21 km/h
THIV criterion	n/a	$\|21\text{ km/h} - 19\text{ km/h}\| \leq 3$ km/h; fulfilled
Time of flight of TH	0.15 s	0.16 s
Time of flight of TH criterion	n/a	$\|0.16\text{ s} - 0.15\text{ s}\| \leq 0.05$ s; fulfilled
Length of flight of TH	n/a	0.40 m
Length of contact	20 m	17 m
Duration of contact	0.71 ± 0.02 s	0.75 s
Exit box criterion	fulfilled	fulfilled
Maximum permanent deflection	0.76 ± 0.01 m (post no. 10)	0.67 m (post no. 11)
Number of damaged posts	12 (post nos. 7–18)	13 (post nos. 7–19)

Analysis of the deflection of a barrier during a crash is vital. Such an analysis was conducted based on the results of the numerical simulation. Here, Fig. 7 presents the maximum dynamic lateral positions of the subsystems of the considered barrier and car during the collision, which are calculated from the undeformed traffic side of the barrier (i.e., similar to the determination of the working width value). For the purpose of analysis, these values were called the dynamic working width (i.e., the time variation of the working width). Consequently, the maximum value from all these curves was considered as the value of the working width. The negative values for the car for time $t < 0.0$ s meant that the car was approaching the barrier (before the impact). Similarly, the negative values for the time $t \geq 0.74$ s meant that the car left the barrier and crossed the vertical surface defined by the position of the undeformed traffic face of the barrier (i.e., before the impact). Immediately after the impact, in the first phase of the crash, all the analyzed components (cables, posts, and cars) deflected similarly. Consequently, they had similar dynamic working width values (Fig. 7). At time $t = 0.04$–0.05, the posts were bent such that cables detached from the posts. At the moment of cable detachment, the dynamic working width of the posts was 15 cm greater than that of the cables, and 12 cm greater than that of the car, as shown in Fig. 7. As the car continued to push into the barrier, the successive posts began to rotate and then began to bend toward the ground. The cables made contact with the car and locally deformed the car body. This mechanism enables cables to efficiently contain and guide cars. As the car continued to move, the next posts were hit and bent to the ground, and subsequently, they went under the

vehicle. That is also visible in Fig. 7 at time t = 0.06–0.56 s, that is, the values of the dynamic position of the posts (approximately 0.66 m) are smaller than those for the car and the cables. At time t = 0.19 s, the dynamic lateral position of the car front reached its maximum. Next, the barrier began to rotate and redirect the car back toward the road. Then, at time t = 0.30 s, the rear end of the car impacted the barrier for the second time in the place that had been previously damaged by the front end of the car. The two aforementioned impacts are illustrated in Fig. 7. It is worth noting that a similar phenomenon occurred in crash tests with long vehicles such as buses. First, the front of the vehicle impacted a barrier, and subsequently, the rear of the vehicle hits the previously damaged section again (Wilde et al., 2017). In the analyzed crash test, the second impact of the rear end resulted in the cables and vehicle reaching their maximum dynamic working widths. The object with the greatest dynamic lateral position was the car, and this value determined the working width W_m = 1.28 m at time t = 0.30 s. The maximum lateral position of the cables was 1.25 m, which was 3 cm smaller than that of the car. This is because the cables cut into the body of the vehicle during the crash. A similar effect was observed in the full-scale crash test, and it is discussed in the section concerning the car damage (Section 3.1.4). It is worth mentioning that the deflection of the bottom cable was greater than those of the middle and top cables. In the gray box shown in Fig. 7, the maximum values of the dynamic working width for the considered subparts are summarized.

Here, Fig. 8 shows the yaw angle of the car, wherein the yaw angles for the selected time steps are depicted in the boxes. After the strike, in the first phase (time t = 0.0–0.3 s), the actual vehicle rotated clockwise up to 21.1°, and in the simulation, the maximum yaw angle was 22.8°. Next, at time t > 0.30 s, the vehicle was forced back onto the road by the barrier. In the second phase, the vehicle began to turn counterclockwise. In the full-scale crash test, the car left the barrier at time t = 0.71 s. In the simulation, this occurred at time t = 0.75 s. As observed in. Fig. 8, the values of the yaw angle during the contact between the car and the barrier (time from 0.0 to 0.75 s) were similar in the actual test and the simulation. In the crash test, at time t = 0.8 s, the longitudinal axis of the car coincided with the original direction of impact, that is, the yaw angle of the car was 0°. In the simulation, this happened at time t = 1.0 s. Next, the car continued to rotate counterclockwise as observed from the graphs in Fig. 8 and the snapshots in Fig. 5 and Fig. 6. After departure from the barrier, the car in the full-scale test experienced greater rotations than that in the simulation. The differences in the behavior of the car after leaving the barrier may result from, among others, the age and technical conditions of the vehicle. Finally, the subpart with the highest value of the lateral position was the post, and they determined the static (permanent) working width. In the actual test, the static working width equaled 0.76 m for post no. 10, and in the simulation, it was 0.67 m for post no. 11.

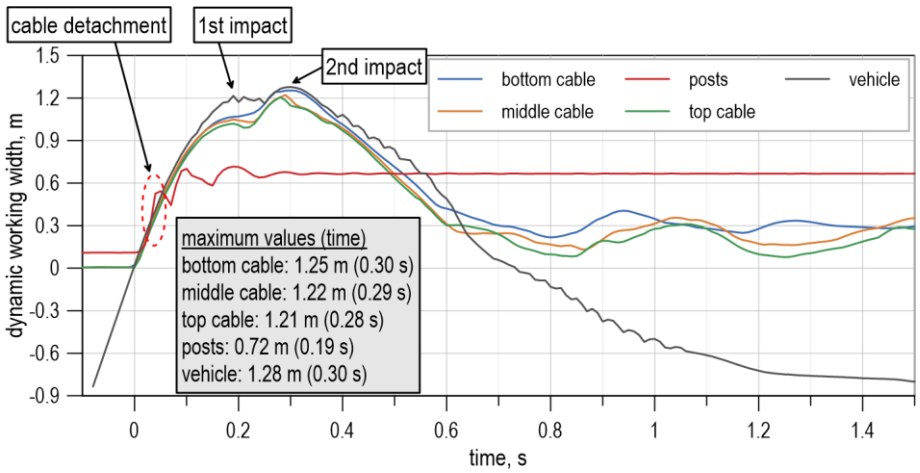

Fig. 7 Maximum dynamic lateral positions of subsystems during crash calculated from undeformed traffic side of barrier (dynamic working width).

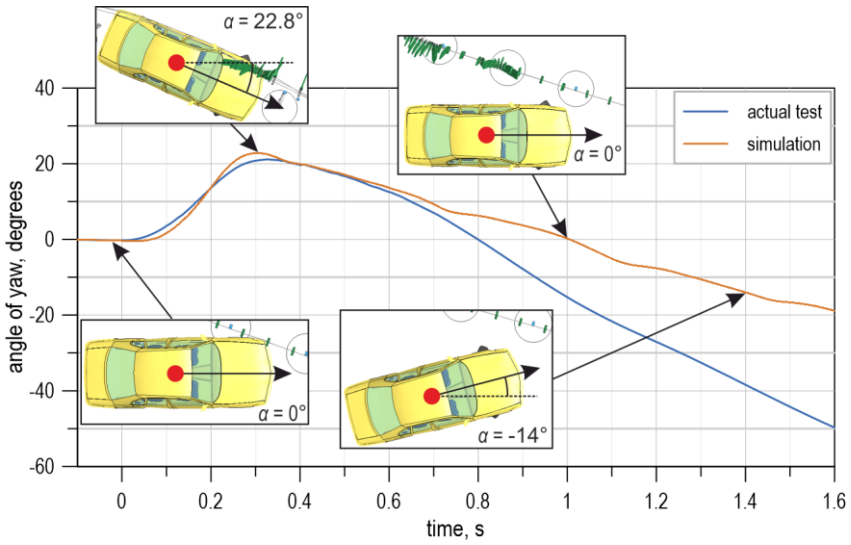

Fig. 8 Variations in yaw angle

Assessing the effects of a crash on people inside an impacting vehicle is a key aspect. As previously mentioned, the impact severity level was determined by the ASI and THIV values. The variations in these two severity indices are shown in Fig. 9. In the graph of ASI, Fig. 9-a, the first peak is for the crash into the first posts after the impact point, that is, post no. 10. The next peaks represent the impacts of the car into successive posts. For both the actual and the numerical tests, the maximum ASI value occurred when the car collided with post no. 13. In the crash test, the ASI was equal to 0.52 at time t = 0.24 s, and in the simulation, the ASI was 0.51 at time t = 0.28 s. The THIV in the crash test was 19 km/h, and in the simulation, it was 21 km/h. Because ASI and THIV are important indices, their graphs were additionally verified using ANOVA and Sprague-gear metrics, which were implemented in the RSVVP software ("Roadside Safety Verification and Validation Program RSVVP, www.roadsafellc.com/NCHRP22-24/RSVVP/, date of access 01.02.2018," 2018). The metrics are listed in Tab. 4. The values of the metrics allow us to conclude that the ASI and THIV curves from the crash test and simulation are similar. The obtained ASI and THIV values indicate that the barrier provided the highest impact severity level of A (ASI < 1.0; THIV < 33 km/h).

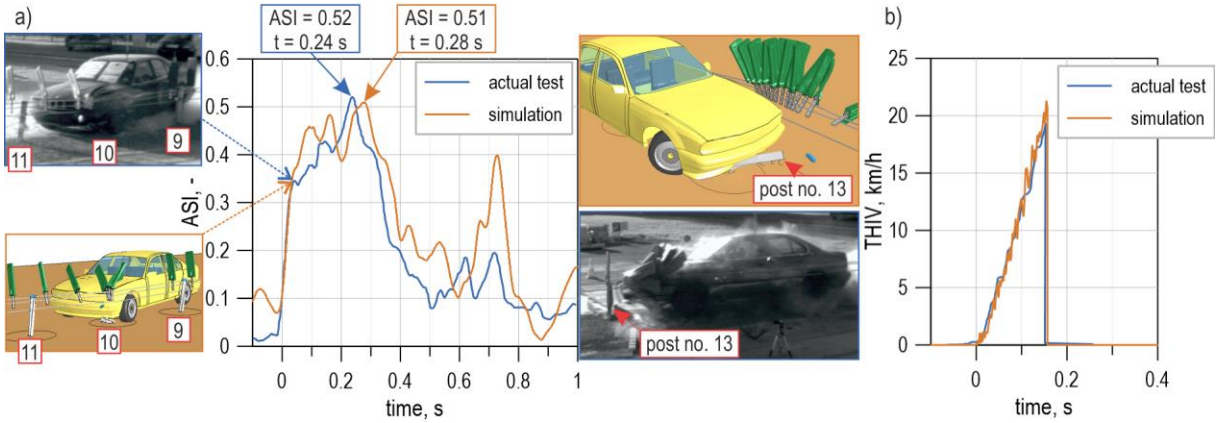

Fig. 9 Impact severity indices: a) ASI and b) THIV.

Tab. 4 Comparison of ASI and THIV curves.

Metrics		ASI	THIV	Criteria[a]
Single value	Regression coefficient	0.835	0.739	n/a
	Correlation coefficient	0.904	0.805	n/a
ANOVA	Average	0.092	0.019	≤0.05
	Standard deviation	0.124	0.205	≤0.35

MPC	Sprague–Geers magnitude	0.166	0.106	≤0.40
	Sprague–Geers phase	0.083	0.161	≤0.40
	Sprague–Geers comprehensive	0.186	0.192	≤0.40

[a] (Ray, 2011)

3.1.3. Damage to cable barrier

The overall view of the damage to the system in the simulation is similar to that obtained in the crash test. The static working width of each post is shown in Fig. 10. The wire ropes did not rapture in the actual test or simulation. A general view of the barrier after a crash is shown in Fig. 11.

In the full-scale crash test, 12 posts were damaged owing to the collision, that is, from post no. 7 to post no. 18. Therefore, the length of damage to the barrier was 22 m. Posts nos. 7, 8, 9, and 18 were slightly rotated and tilted from their vertical positions, and post nos. 10–17 were bent to the ground. The maximum static working width after the test was measured for post no. 10 and it was 0.76 m (see Fig. 10-a), and it was the first post after the impact point. The wire ropes detached from post nos. 9–17. During the crash, the car pushed the anti-glare screens to one place located between post nos. 14–16, which can be seen on the right-hand side in Fig. 11-a.

In the numerical simulation, post nos. 7–19 were damaged; hence, the number of damaged posts was 13. The crash resulted in damage of 24 m length in the barrier. Post nos. 10–16 were bent to the ground. Post nos. 8, 9, 17, and 18 were rotated and bent, but were not completely bent to the ground. Post nos. 7 and 19 were only slightly rotated and deflected. The maximum static working width was obtained using post no. 11, and the value was 0.67 m. This was the second consecutive post after the impact point. Subsequently, the cables detached from post nos. 8–17. Similar to the actual crash test, the anti-glare screens were moved along the cables by the car. After the crash, the anti-glare screens were shifted and located between post nos. 17–19. A few screens were left at post nos. 11, 12, 14, and 16. A view of the damaged barrier from the simulation is shown in Fig. 11-b.

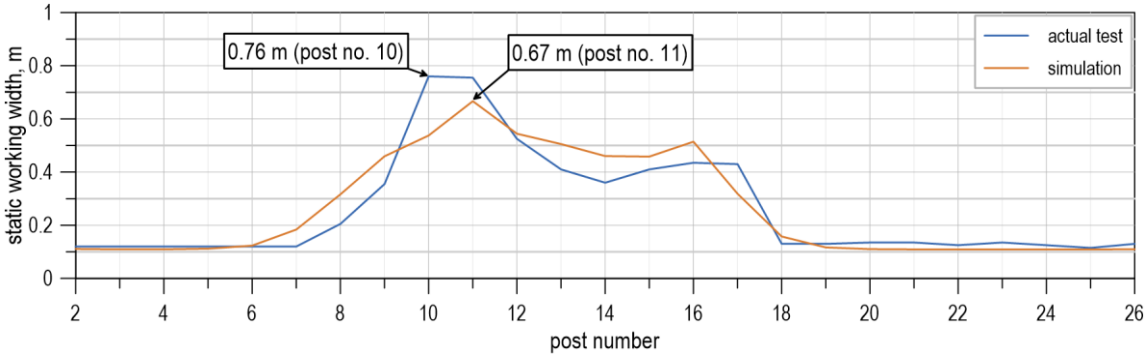

Fig. 10 Static (permanent) working width for posts.

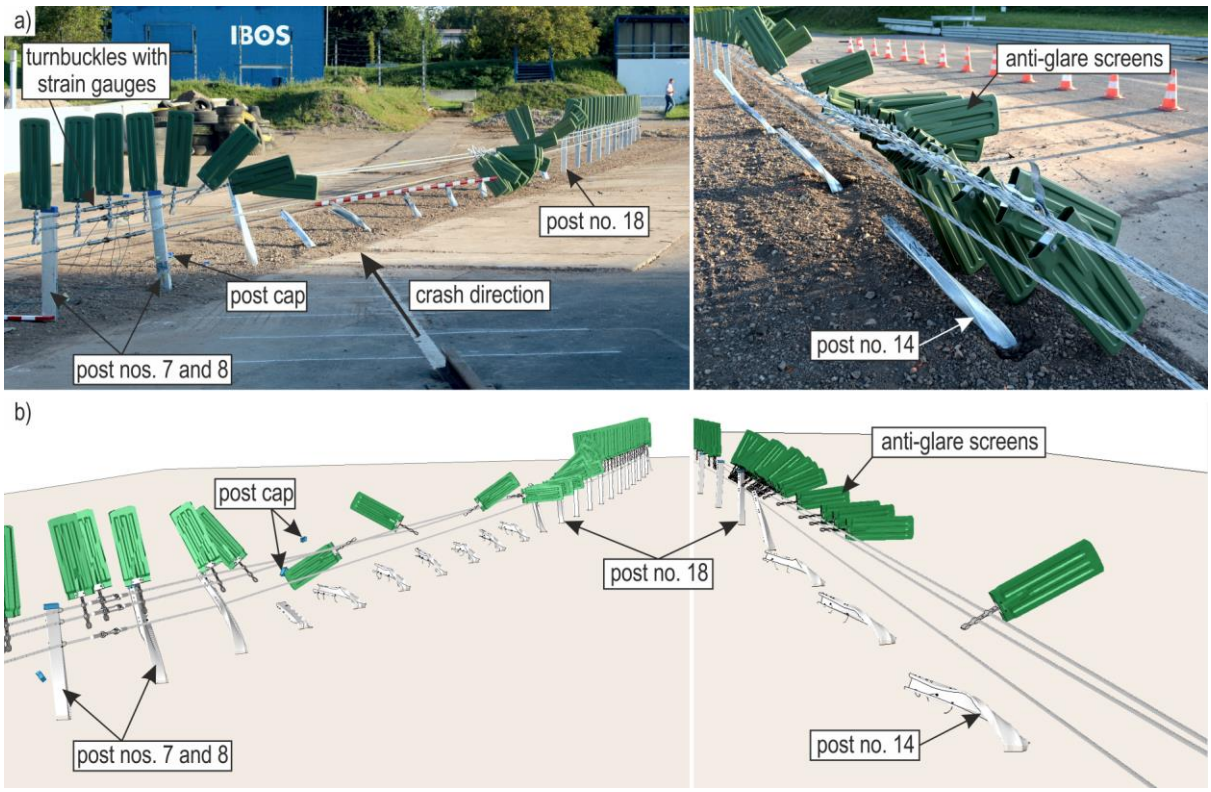

Fig. 11 General view of barrier after the collision: a) full-scale crash test and b) simulation.

Both the actual test and the simulation revealed the specific mechanism of the deformation of the posts. After the impact, the cables began to deflect. This caused the post to rotate and bend. On average, this concerned the two posts in front of the car to which the car had not yet reached, that is, the car had not yet made contact with them. Simultaneously, the cables began to detach from the post. The mechanism is shown in Fig. 12. From this figure, it can be seen that the car was impacting post no. 11. Simultaneously, the next post, that is post no. 12, started rotating and bending. This resulted from the action of the horizontal forces from the cables. Post no. 13 also began to rotate. Subsequently, the vehicle impacted these posts, causing them to bend to the ground. Therefore, after the collision, some of the posts were slightly rotated and bent, and some posts were completely bent to the ground. The first group included the posts affected only by the deflected cables that had no contact with the car or the contact was at the moment of the impact or when the car departed from the barrier. An example of the post-impact deformation of such posts is shown in Fig. 13-a. The posts hit directly by the car were bent to the ground, as shown in Fig. 13-b.

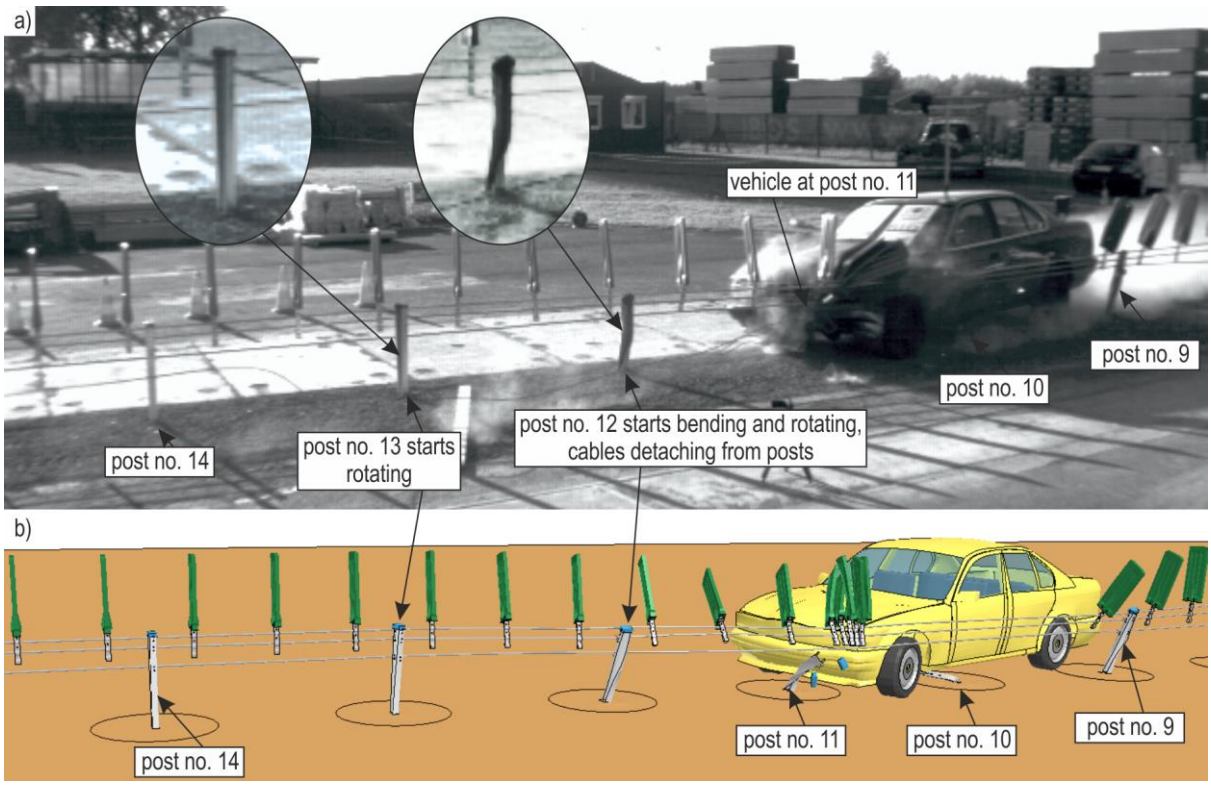

Fig. 12 Mechanism of deformation of the posts during the crash: a) crash test and b) simulation.

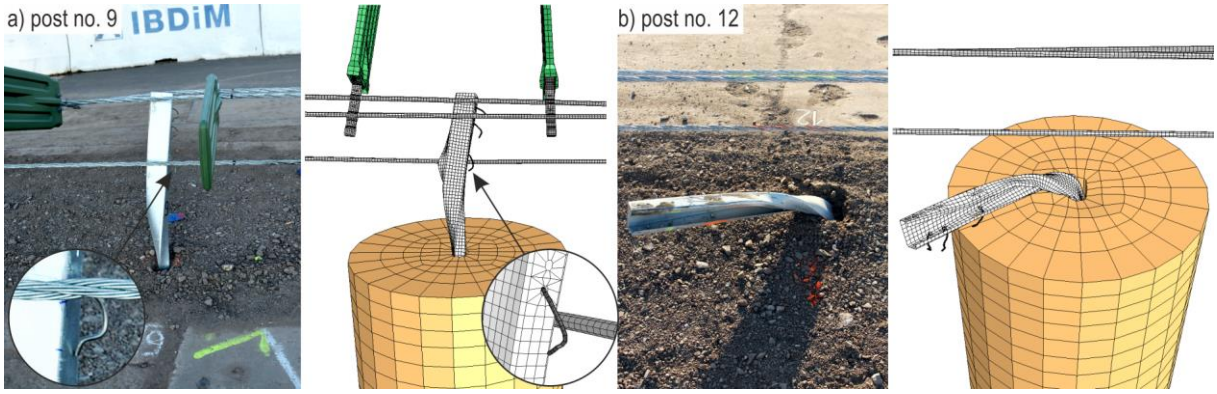

Fig. 13 Comparison of damage to posts: a) post no. 9 – rotated and bent and b) post no. 12 – bent to the ground.

3.1.4. Damage to vehicle

A comparison of the damage to the numerical car model and actual car is shown in Fig. 14. In the crash test, the front left of the car, including the bumper, fender, hood, and wheel, was damaged. The deformation along the left side of the car body, at the height between the wheel and door handles, was caused by the cables. The left side of the rear bumper was detached. The left-wing mirror was damaged; however, it did not detach from the car. The front and rear lamps on the left were broken.

In the simulation, the front of the car was damaged, similar to the actual car. The maximum value of the effective plastic strain was 0.254, and the area of damage was limited to the front left. There was no deformation of the cables along the left side of the car, as observed in the actual test. This is because of the simplified car model, and the average size of the shell FE side was approximately three times the diameter of the wire rope. Therefore, the model used did not capture all details of the damage. The VCDI index was LS0000000 in both actual and numerical tests.

Fig. 14 Damage to the vehicle: a) crash test and b) simulation.

3.2. Analysis of axial forces in turnbuckles during crash

The strains in the turnbuckles were measured during the actual impact test using six strain gauges. Here, Fig. 3-b shows the strain gauges on the actual system. Strain gauges 1 and 2 measured the strains in the top turnbuckle, gauges 3 and 4 in the middle turnbuckle, and gauges 5 and 6 in the bottom turnbuckle. Therefore, two strain gauges were installed on each turnbuckle. These measurements allowed for the determination of the forces in the turnbuckles. It was assumed that the forces in the cables were the same as those in the turnbuckle. The results are shown in Fig. 15.

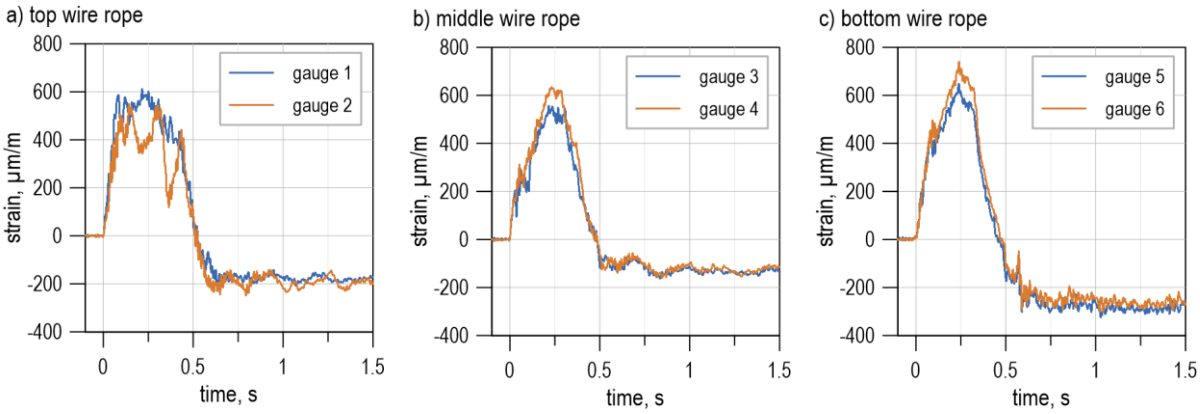

Fig. 15 Strain vs. time curves from the crash test: a) top turnbuckle, b) middle turnbuckle, and c) bottom turnbuckle.

To obtain the values of the axial forces in the cables, laboratory tests on the turnbuckles were conducted using a universal testing machine (UTM). The test stand and specimens are shown in Fig. 16. The forces in the turnbuckle were acquired from the UTM and the strains from the strain gauge. These tests were used to determine the force–strain relationship, which allowed for the assessment of the axial forces in the cables during the crash. Furthermore, Fig. 17 presents a comparison of the forces in the turnbuckles obtained from the crash test and simulation, and Tab. 5 summarizes the maximum forces and the time of their occurrence. For the purpose of analysis, the greater force determined from the two strain gauges for each turnbuckle was chosen as the maximum force in the cable. Furthermore, Fig. 18 shows a comparison of the summation of axial

forces in cables over time obtained in the simulation and crash test. The values from the test were calculated as the sum of the values from the strain gauges for which the maximum forces for the cables were obtained, i.e., from strain gauges 1, 4, and 6.

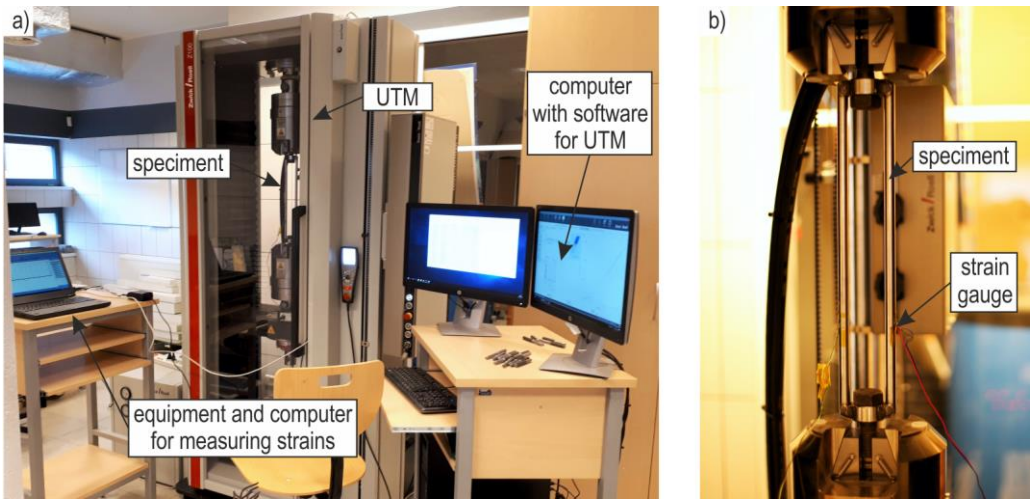

Fig. 16 Laboratory tests of turnbuckle: a) test stand and b) turnbuckle with strain gauge.

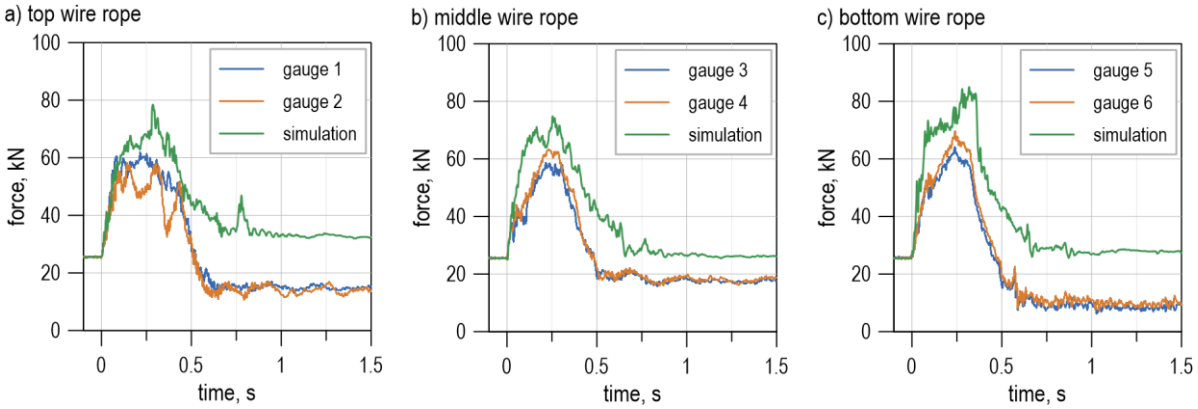

Fig. 17 Comparison of axial forces in cables from numerical simulation and crash test: a) top cable, b) middle cable, and c) bottom cable.

Tab. 5 Comparison of axial forces in cables and time of their occurrences from numerical simulation and crash test.

Turnbuckle/wire rope	Location of measurement	Force, kN	Time of occurrence, s
Turnbuckle at the top wire rope	Strain gauge 1	61.96	0.22
	Strain gauge 2	58.18	0.14
	Numerical simulation	78.50	0.29
Turnbuckle at the middle wire rope	Strain gauge 1	58.64	0.22
	Strain gauge 2	63.28	0.23
	Numerical simulation	74.81	0.25
Turnbuckle at the bottom wire rope	Strain gauge 1	64.09	0.24
	Strain gauge 2	69.59	0.24
	Numerical simulation	85.00	0.32

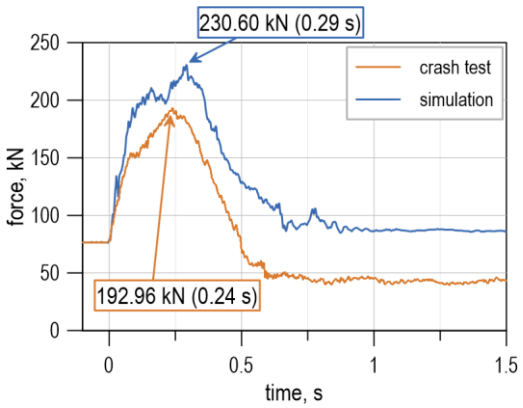

Fig. 18 Comparison of total axial force in cables from numerical simulation and crash test.

The results from the crash test indicate that a maximum force of 69.59 kN was exerted on the bottom cable. This force was approximately 2.7 times greater than the initial pre-tension force. The forces in the middle and top cables were similar and were approximately 10% lower than those in the bottom cable. Similar conclusions can be drawn from the simulation results; however, the forces from the simulation were greater than those from the crash by 18–27%. The time of occurrence of the maximum force (t = 0.24 s in the actual test; t = 0.32 s in the simulation) corresponded to the time of occurrence of the working width (t = 0.30 s). At time t = ~0.3 s, the forces first increased and, then decreased. After the departure of the car from the barrier, the cables remained in tension. For comparison, a report (Schmidt et al., 2013) that shows the results of the test in which a 2,267 kg pickup truck impacted a low-tension three-cable barrier installed on a road curve with a radius of 134 m at a speed of 101.6 km/h and at an angle of 21.6° (impact kinetic energy was 122.3 kJ) is presented. They report that the maximum cable load during this impact was 65.55 kN, which occurred 0.241 s after the impact.

Measurements from the considered crash test revealed that, after the collision, the force in the bottom rope was approximately 14.5 kN; in the middle cable, approximately 18.1 kN; and in the bottom cable, approximately 9.9 kN. In the simulation, these values were 33.0, 25.7, and 27.6 kN, respectively. The decrease in the cable force in the actual system was due to the change in the curvature of the wire ropes in the secant between the posts supporting the ropes after the crash. It is also suspected that the decrease in the force could be generated by the small movement of the anchor in the soil; however, these movements were not measured in situ. In the numerical test, the forces in the cables after the collision were greater than the initial pre-tension force. This resulted from the simplified anchor–soil interaction model in which the anchors were fixed; hence, the movement of the anchor was not possible. It is also worth noting that the axial forces were significantly lower than the breaking load of the cable, which was approximately 210 kN (Bruski, 2020; Reid et al., 2010).

3.3. Influence of anti-glare screens on cable arrangement

In the crash test, anti-glare screens were installed on the cables. As described in Section 3.1.3, these screens slid along the wire ropes during collision; however, none of the screens was detached from the cables, as shown in Fig. 11. Analyzing the actual test and simulation results, it was observed that the two top cables were held by the screens at a constant distance during the crash. Based on our experience, in tests without anti-glare screens, the top cable tends to slide over the hood and stop on the wing mirror. Even if the mirror breaks, the cables can still be held effectively and do not slide higher on the A-pillar. However, it may occur in real-life accidents where cables can slide higher, even damaging the roof, especially in crashes with significant impact energies (Stolle and Reid, 2015).

Here, Fig. 19 shows examples of the behavior of the cables during collisions. The first example, Fig. 19-a, presents the crash test of a cable barrier with anti-glare screens. As mentioned previously, the wire ropes were kept on the screens at a constant distance during the collision. Behind the car, three cables were visible at a height below the top surface of the tailgate, as depicted in Fig. 19-a. The positions of the cables during the crash can also be inferred from the damage to the car body, as shown in Fig. 14-a. Furthermore, Fig. 19-b-c shows two other examples of crash tests with a cable barrier and a passenger car. It is emphasized that these two tests are not the subject of this research, but they are presented only to show the behavior of the wire ropes in tests without anti-glare screens. Moreover, Fig. 19-b shows a modified TB32 crash test in which the impact angle was altered from 20° to 7° (Bruski et al., 2019), and Fig. 19-c presents the TB32 test with a barrier without anti-glare screens. In both tests, the two bottom cables were kept above the wheels while the top cable slid to the wing mirror. This observation is important because most numerical models of cars do not have wing mirrors. To improve the behavior of cables in numerical simulations, it may be necessary to add such mirrors.

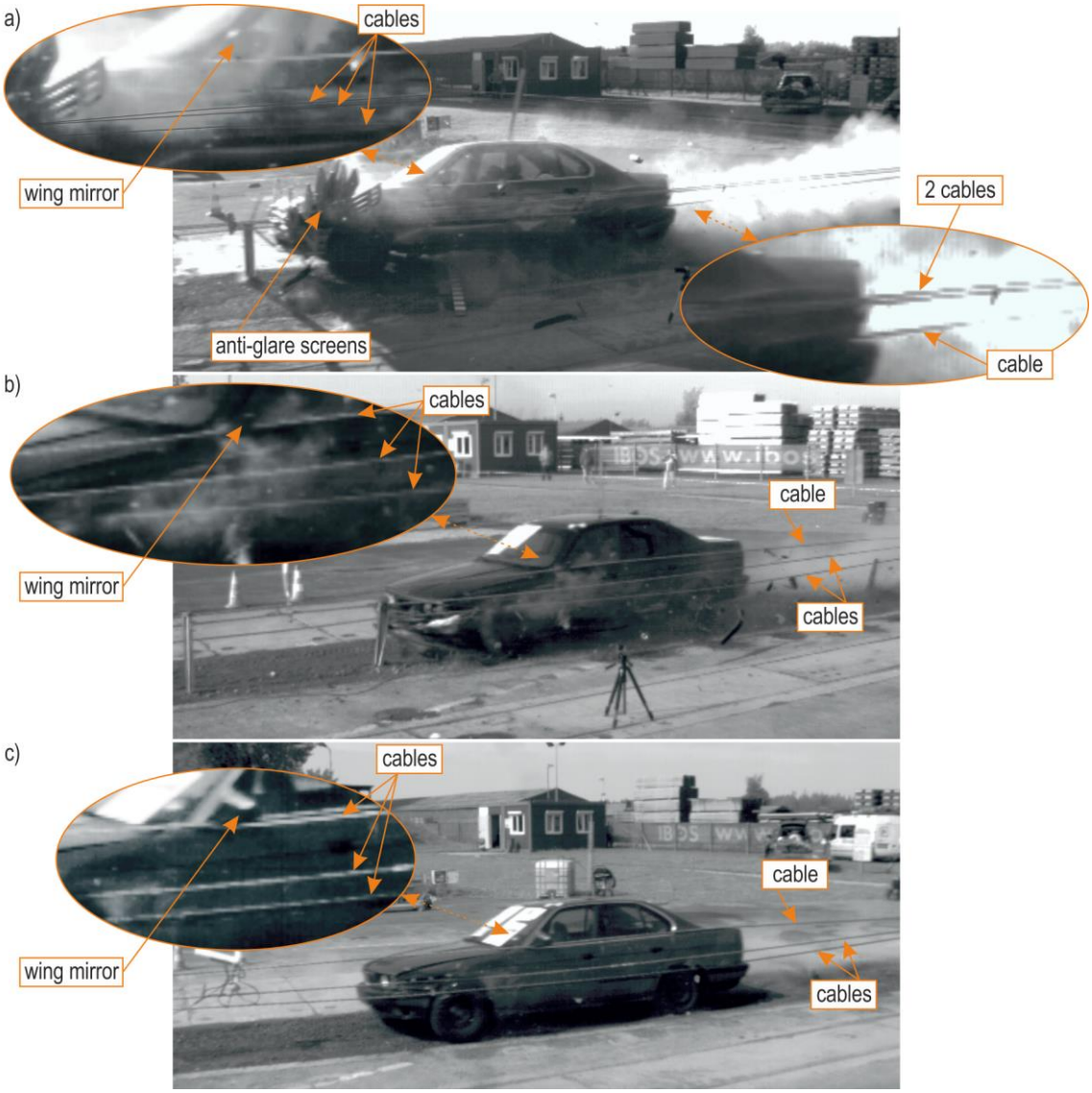

Fig. 19 Behavior of the cables during collision: a) crash test with anti-glare screens, b) modified TB32 test with no screens, and c) TB32 test with no screens.

3.4. Energy analysis

The energy balance obtained from the numerical simulation is shown in Fig. 20-a. The total energy spent throughout the crash event was constant and equaled 750 kJ. At the moment of the car departing from the barrier (vertical dashed grey lines in Fig. 20), the kinetic energy was 33.5% of the total energy; contact energy, 32.1%; and internal energy, 28.4%. After the departure of the car from the barrier, internal energy remained approximately constant. However, the kinetic energy, which mainly consisted of the kinetic energy of the vehicle, decreased because of the reduction in the speed of the vehicle owing to the frictional forces between the tires and the ground. This, in turn, causes an increase in the contact energy. The hourglass energy (black dotted line) was at a low level in relation to the other components of the energy, which satisfied the criteria included in the report ("PN-EN 16303:2020. Road restraint systems - Validation and verification process for the use of virtual testing in crash testing against vehicle restraint system," 2020).

Here, Fig. 20-b shows the amount of absorbed energy owing to the deformation and damage to the parts of the barrier and vehicle. The posts, hooks, cables, soil, and vehicle were considered. In the first phase of the impact, to the moment of working width occurrence (t = 0.30 s), most of the impact energy was absorbed by the posts (54.9 kJ) and the cables (45.6 kJ). After the maximum lateral deflection of the cables was reached, the vehicle began to be pushed back onto the road, and the wire ropes began to return part of the absorbed energy to the vehicle. At the moment of departure of the car from the barrier, the posts absorbed 36.6% of the total absorbed energy (the average amount of absorbed energy by one damaged post was 6 kJ); the car, 21.5%; the cables, 20.4%; the soil, 8.2%; and the hooks, 2.4%. After leaving the barrier, only the internal energy of the car increased.

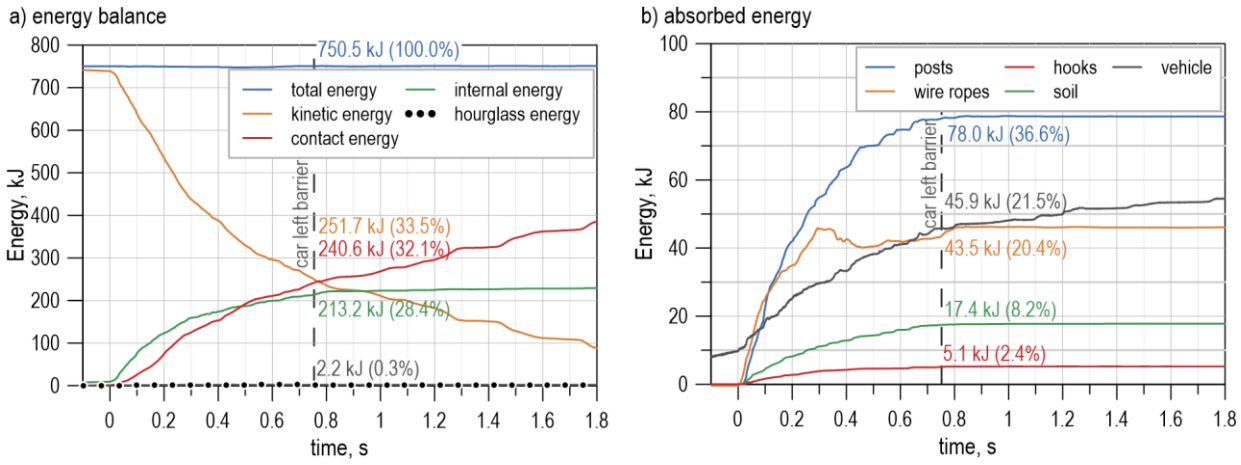

Fig. 20 Energy analysis in the numerical simulation: a) energy balance and b) energy absorption by the subparts of the system.

3.5. Summary of experimental and numerical research

Based on these results, it can be concluded that the numerical simulation corresponds well with the full-scale crash test. The trajectories of the vehicles are similar, and the damage to the barrier from the simulation and actual test is comparable. The crash test indices such as the working width, ASI, and THIV have similar values.

The differences between the crash test and the simulation can be attributed to several factors. The mass of the car used in the actual crash test was smaller than that in the simulation by 61.2 kg. Consequently, the value of the working width from the simulation was higher than that from the crash test, whereas the ASI was slightly lower. The difference in the mass of the car could also have affected the number of damaged posts. In the simulation, one post more than that in the real test was damaged (post no. 19). Because a greater working width was obtained in the simulation than in the actual test, the axial forces in the cables were also greater in the

simulation. However, the difference in the car mass is not the only reason for the discrepancies in cable forces. The computational model of the barrier assumed a full constraint of the concrete anchor blocks, which made it impossible to shorten the cable length. Hence, the forces in the simulation could not decrease below the initial pretension force. In reality, even a small movement of the anchors in the ground causes a reduction in cable tension. However, the aforementioned aspects do not imply that the vehicle and barrier responses from the simulation are incorrect.

It should also be noted that a full-scale crash test itself is not a completely reproducible test; that is, by carrying out a new crash test with the same road safety barrier, same vehicle model, same test site, and same laboratory staff, the results obtained can be different (Ray, 2011). Therefore, the accuracy of the simulation with a crash test should be assumed at a reasonable level of agreement.

4. SUMMARY AND CONCLUSIONS

The study presents the analysis of the collision of a 1,500 kg passenger car with a 3-cable high-tension barrier installed on a horizontal road curve with a radius of 400 m. A less favorable case of impact, that is, the impact on the convex side of the barrier, was considered. The impact speed was 110 km/h and the impact angle was 20°. As part of this study, a numerical model of the cable barrier was developed and validated against the results of a full-scale crash test. Good agreement was obtained between the simulation and the actual crash test results. The analyses allowed for a comprehensive evaluation of the responses of both the cable barrier and the car during collision. The most important findings are as follows:

- This study proved that the cable barrier could properly restrain and redirect the impacting car back onto the road, while ensuring the highest level of safety.
- The wire ropes detached from the posts before the car made contact with them. The detached cables caused the posts to rotate and bend. The car then hit the previously deformed posts and bent them to the ground.
- The maximum force during the crash occurred in the bottom cable. The maximum force was approximately 40% of the cable-breaking load. After the collision, the cables were still in tension; however, the force was less than the initial pre-tension force.
- The posts absorbed the largest amount of energy, which was 36.6% of the total energy absorbed. For the car, this value was 21.5%.
- The anti-glare screens affected the behavior of the cables. The screens caused the two top cables to be held at a constant distance during the impact. The screens were moved by the car, and no screen was detached from the barrier.
- The applied methods of numerical modeling can effectively reproduce the crash course and obtain reliable values of the indices. As for the limitations of these methods, they affected the values of the forces in the cables, which were greater than those in reality. This was mainly because of the greater weight of the vehicle used in the simulation and the simplified technique of modeling the soil–anchor interaction.

573 The study also confirmed that a numerical model that has undergone the validation process could be a valuable
574 supplement to a full-scale crash test. This verified and validated model can be a rich source of information and
575 can be used in future research.

576 ACKNOWLEDGEMENTS

577 This work was supported by the National Centre for Research and Development (NCBiR) and General Director for
578 National Roads and Motorways (GDDKiA) under the research project "Road Safety Equipment" (contract number
579 DZP/RID-I-67/13/NCBR/2016) and by Grants for Young Scientist from Faculty of Civil and Environmental Engineering
580 at Gdansk University of Technology in 2020. The BWM vehicle model was developed by Transpolis (formerly LIER),
581 the French crash-test house and digital simulation office for road safety equipment. The authors gratefully acknowledge
582 Rafał Kędra (Gdańsk University of Technology) for technical support in the experimental tests of the turnbuckles.
583 Calculations have been carried out at the Academic Computer Centre in Gdańsk, Gdańsk University of Technology,
584 Poland.

585 REFERENCES

586 AASHTO MASH-2, Manual for assessing safety hardware (MASH), 2nd edition, American Association of
587 State Highway Transportation Officials, 2016.
588 Alberson, D.C., Bligh, R.P., Buth, C.E., Bullard, D.L., 2003. Cable and Wire Rope Barrier Design
589 Considerations: Review. Transp. Res. Rec. 1851 , 95–104. doi:10.3141/1851-10
590 Bi, J., Fang, H., Weggel, D.C., 2010. Finite element modelling of cable median barriers under vehicular
591 impacts. WIT Trans. Built Environ. 113, 219–230. doi:10.2495/SU100191
592 Bruski, D., 2020. Determination of the bending properties of wire rope used in cable barrier systems. Materials
593 (Basel). 13 17 . doi:10.3390/ma13173842
594 Bruski, D., Burzyński, S., Chróścielewski, J., Jamroz, K., Pachocki, Ł., Witkowski, W., Wilde, K., 2019.
595 Experimental and numerical analysis of the modified TB32 crash tests of the cable barrier system. Eng.
596 Fail. Anal. 104, 227–246. doi:10.1016/j.engfailanal.2019.05.023
597 Budzyński, M., Jamroz, K., Jeliński, L., Bruski, D., Pachocki, Ł., 2022. Assessing Roadside Hybrid Energy
598 Absorbers Using the Example of SafeEnd. Materials (Basel). 15 1712 , 1–21. doi:10.3390/ma15051712
599 Chen, L., Xiao, Y., Xiao, G., Liu, C., Agrawal, A.K., 2015. Test and numerical simulation of truck collision
600 with anti-ram bollards. Int. J. Impact Eng. 75, 30–39. doi:10.1016/j.ijimpeng.2014.07.011
601 Cooner, S.A., Rathod, Y.K., Alberson, D.C., Bligh, R.P., Ranft, S.E., Sun, D., 2009. Development of
602 guidelines for cable median barrier systems in Texas.
603 Fang, C., Rasmussen, J.D., Bielenberg, R.W., Lechtenberg, K.A., Faller, R.K., Linzell, D.G., 2021.
604 Experimental and numerical investigation on deflection and behavior of portable construction barrier
605 subjected to vehicle impacts. Eng. Struct. 235 May . doi:10.1016/j.engstruct.2021.112071
606 Fang, H., Wang, Q., Weggel, D.C., 2015. Crash analysis and evaluation of cable median barriers on sloped
607 medians using an efficient finite element model. Adv. Eng. Softw. 82, 1–13.
608 Hallquist, J., 2006. LS-DYNA, Theory Manual.
609 Honda, M., Kawamura, C., Kizaki, I., Miyajima, Y., Takezawa, A., Kitamura, M., 2021. Construction of
610 design guidelines for optimal automotive frame shape based on statistical approach and mechanical
611 analysis. C. - Comput. Model. Eng. Sci. 128 2 , 731–742. doi:10.32604/cmes.2021.016181
612 Klasztorny, M., Zielonka, K., Nycz, D.B., Posuniak, P., Romanowski, R.K., 2018. Experimental validation of
613 simulated TB32 crash tests for SP-05/2 barrier on horizontal concave arc without and with composite
614 overlay. Arch. Civ. Mech. Eng. 18, 339–355.
615 Marzougui, D., Kan, C.D., McGinnis, R., Opiela, K.S., 2009. Analyzing the Effects of End-Anchor Spacing
616 and Initial Tension on Cable Barrier Deflection Using Computer Simulation. NCAC Work. Pap. 1–12.

617 Marzougui, D., Mahadevaiah, U., Tahan, F., Kan, C.D., McGinnis, R., Powers, R., 2012. NCHRP Report 711,
618 Guidance for the Selection, Use, and Maintenance of Cable Barrier Systems.
619 Mohan, P., Marzougui, D., Meczkowski, L., Bedewi, N., 2005. Finite element modeling and validation of a 3-
620 strand cable guardrail system. Int. J. Crashworthiness 10 3 , 267–273. doi:10.1533/ijcr.2005.0345
621 National Crash Analysis Center, http://www.ncac.gwu.edu/vml/models.html, date of access 10.03.2016
622 [WWW Document], 2016.
623 Pachocki, L., Bruski, D., 2020. Modeling, simulation, and validation of a TB41 crash test of the H2/W5/B
624 concrete vehicle restraint system. Arch. Civ. Mech. Eng. 20 62 , 1–23. doi:10.1007/s43452-020-00065-
625 7
626 PN-EN 1317-1:2010. Road restraint systems – part 1: Terminology and general criteria for test methods, 2010.
627 PN-EN 1317-2:2010. Road restraint systems – part 2: Performance classes, impact test acceptance criteria and
628 test methods for safety barriers including vehicle parapets, 2010.
629 PN-EN 1317-5+A2:2012. Road restraint systems – part 5: Product requirements and evaluation of conformity
630 for vehicle restraint system, 2012.
631 PN-EN 16303:2020. Road restraint systems - Validation and verification process for the use of virtual testing
632 in crash testing against vehicle restraint system, 2020.
633 Qian, G., Massenzio, M., Ichchou, M., 2016. Development of a W-Beam Guardrail Crashing Model by
634 considering the Deformations of Components. Proc. 5th Int. Conf. Mechatronics Control Eng. - ICMCE
635 ’16 42–46.
636 Ray, M.H., 2011. Procedures for Verification and Validation of Computer Simulations Used for Roadside
637 Safety Applications, Procedures for Verification and Validation of Computer Simulations Used for
638 Roadside Safety Applications. doi:10.17226/17647
639 Ray, M.H., Silvestri, C., Conron, C.E., Mongiardini, M., 2009. Experience with cable median barriers in the
640 United States: Design standards, policies, and performance. J. Transp. Eng. 135 10 , 711–720.
641 doi:10.1061/(ASCE)TE.1943-5436.0000047
642 Reid, J.D., Kuipers, B.D., Sicking, D.L., Faller, R.K., 2009. Impact performance of W-beam guardrail installed
643 at various flare rates. Int. J. Impact Eng. 36 3 , 476–485. doi:10.1016/j.ijimpeng.2008.08.006
644 Reid, J.D., Lechtenberg, K., Stolle, C.S., 2010. Development of Advanced Finite Element Material Models for
645 Cable Barrier Wire Rope.
646 Roadside Safety Verification and Validation Program RSVVP, www.roadsafellc.com/NCHRP22-24/RSVVP/,
647 date of access 01.02.2018 [WWW Document], 2018.
648 Schmidt, T.L., Lechtenberg, K.A., Meyer, C.L., Faller, R.K., Bielenberg, R.W., Reid, J.D., Sicking, D.L.,
649 2013. Evaluation of the New York Low-Tension Three-Cable Barrier on Curved Alignment.
650 Sheikh, N.M., Alberson, D.C., Chatham, L.S., 2008. State of the practice of cable barrier systems. Transp. Res.
651 Rec. 2060 , 84–91. doi:10.3141/2060-10
652 Stamatiadis, N., Sagar, S., Wright, S., Green, E., Souleyrette, R., 2021. Cable median barrier effect on
653 commercial vehicle crossover crashes. Transp. Res. Rec. 2675 9 , 1423–1433.
654 doi:10.1177/03611981211007845
655 Stolle, C.S., Reid, J.D., 2015. Compatibility of passenger vehicles and cable median barrier systems. ASME
656 Int. Mech. Eng. Congr. Expo. Proc. doi:10.1115/IMECE2017-70557
657 Stolle, C.S., Reid, J.D., 2011. Development of a wire rope model for cable guardrail simulation. Int. J.
658 Crashworthiness 16 3 , 331–341. doi:10.1080/13588265.2011.586609
659 Teng, T., Liang, C., Tran, T., 2016. Development and validation of a finite element model for road safety
660 barrier impact tests. Simul. Trans. Soc. Model. Simul. Int. 92 6 , 565–578.
661 Uddin, W., 2004. Crashworthiness analysis and simulations of vehicles impacting a roadside guardrail. C. -
662 Comput. Model. Eng. Sci. 5 3 , 269–278.
663 Wang, Q., Fang, H., Li, N., Weggel, D.C., Wen, G., 2013. An efficient FE model of slender members for crash
664 analysis of cable barriers. Eng. Struct. 52, 240–256. doi:10.1016/j.engstruct.2013.02.027
5 Wilde, K., Bruski, D., Budzyński, M., Burzyński, S., Chróścielewski, J., Jamroz, K., Pachocki, Ł., Witkowski,
6 W., 2019. Numerical analysis of TB32 crash tests for 4-cable guardrail barrier system installed on the
7 horizontal convex curves of road. Int. J. Nonlinear Sci. Numer. Simul. doi:10.1515/ijnsns-2018-0169
8 Wilde, K., Bruski, D., Burzyński, S., Chróścielewski, J., Pachocki, Witkowski, W., 2021. On analysis of
9 double-impact test of 1500-kg vehicle into w-beam guardrail system. Arch. Civ. Eng. 67 2 , 101–115.
0 doi:10.24425/ace.2021.137157
1 Wilde, K., Bruski, D., Burzyński, S., Chróścielewski, J., Witkowski, W., 2017. Numerical crash analysis of
2 the cable barrier. Math. Numer. Asp. Dyn. Syst. Anal. 555–566.
3 Wolny, R., Bruski, D., Budzyński, M., Pachocki, L., Wilde, K., 2022. Influence of a Lighting Column in the

674 Working Width of a W-Beam Barrier on TB51 Crash Test. Materials (Basel). 15 4926 , 1–19.
675 doi:10.3390/ma15144926
676 Wu, W., Thomson, R., 2007. A study of the interaction between a guardrail post and soil during quasi-static
677 and dynamic loading. Int. J. Impact Eng. 34 5 , 883–898. doi:10.1016/j.ijimpeng.2006.04.004
678 Yin, H., Fang, H., Wang, Q., Wen, G., 2016. Design optimization of a MASH TL-3 concrete barrier using
679 RBF-based metamodels and nonlinear finite element simulations. Eng. Struct. 114, 122–134.
680 doi:10.1016/j.engstruct.2016.02.009
681 Yin, H., Xiao, Y., Wen, G., Fang, H., 2017. Design optimization of a new W-beam guardrail for enhanced
682 highway safety performance. Adv. Eng. Softw. 112, 154–164.
683 Zou, Y., Tarko, A.P., Chen, E., Romero, M.A., 2014. Effectiveness of cable barriers, guardrails, and concrete
684 barrier walls in reducing the risk of injury. Accid. Anal. Prev. 72, 55–65. doi:10.1016/j.aap.2014.06.013
685